JACS
JOURNAL OF THE AMERICAN CHEMICAL SOCIETY
pubs.acs.org/JACS
Article

Anion Coordination Transition Enabled by Ion−Dipole Interactions At Low Temperatures

Jingxuan Ren, Dongdong Wang,* Yufeng Chen, Renming Liu, Xinli Guo,* Dan Luo,* and Zhongwei Chen*

Cite This: J. Am. Chem. Soc. 2026, 148, 19128−19137
Read Online

ABSTRACT: While constructing anion-involved solvation structures is key to improving electrolyte performance at low temperatures (LTs), conventional strategies that primarily manipulate Li^+−solvent interactions present significant challenges. These include weakened anion coordination, impeded ion transport, and aggravated interfacial side reactions, making the realization of effective LT operation elusive. Here, we propose a "polarity-contrast" electrolyte design strategy, which enables the construction of a LT-stable, anion-rich solvation structure through deliberate regulation of anion−solvent interactions. The solvent pairs, dimethoxymethane (DMM) and fluoroethylene carbonate (FEC), which exhibits the lowest and highest maximum electrostatic potential, respectively, were selected for electrolyte engineering. At LTs, the weakened interactions between primary solvent DMM and FSI^- promote the coordination of solvation of anions. Meanwhile, the coordinated FEC cosolvent enhances ion−dipole interactions with FSI^-, further anchoring these anions within the solvation sheath. This FSI^--dominated solvation environment facilitates the formation of a fluorine-rich solid electrolyte interphase, which in turn enables uniform Li deposition under LT conditions. Therefore, Li||SPAN full cells demonstrate excellent LT performance, including a high areal capacity of 4.5 mAh cm^{-2} and 150 cycles with 80% retention at −40 °C. Notably, Ah-level Li||SPAN pouch cells demonstrate 50 cycles at −20 °C with exceptional capacity−temperature−lifespan balance, surpassing the most reported LT LMBs.

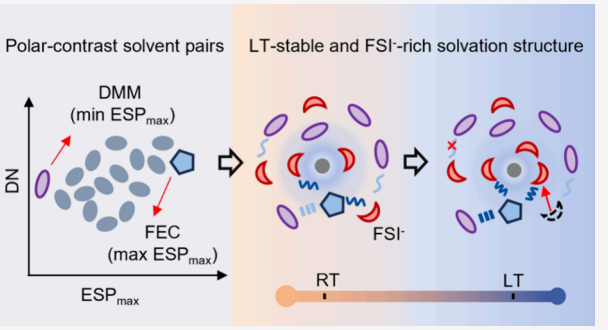

INTRODUCTION

The ubiquitous deployment of lithium metal batteries (LMBs) across electric vehicles and grid-scale renewable energy storage has rendered the resolution of their inadequate low-temperature (LT) performance a critical imperative.[1−3] This operational deficit is primarily attributable to severely hindered ion conduction within bulk electrolytes, kinetically sluggish desolvation and interfacial transport processes, and retarded solid-state diffusion in electrode materials under LT conditions.[4,5] Although externally applied heating strategies can mitigate these limitations by elevating cell operating temperatures, such auxiliary thermal management inevitably incurs substantial penalties in overall energy efficiency and system cost.[6,7]

Beyond electrode structure design and surface modification, electrolyte engineering provides a direct and effective strategy to enhance the LT performance of LMBs.[8,9] Anions exert a pivotal role in ameliorating LT electrochemical performance through multiple mechanisms that encompass restructuring Li^+ transport pathways, mitigating desolvation energy barriers, and enhancing interfacial charge transfer efficiency via solvation behavior.[10] Extensive research endeavors have been dedicated to constructing anion-involved solvation structures by regulating solvent−Li^+ interactions. Specifically, employing weakly solvating solvents attenuates the coordination ability of solvents toward Li^+, thereby elevating the proportion of anions in the solvation sheath.[11−13] In parallel, localized high-concentration electrolytes (LHCE) leverage diluents to engineer localized high-concentration microdomains, forcing anions to participate in the solvation structure and form contact ion pairs (CIP) or ion aggregates (AGG), thereby optimizing ion transport kinetics.[14,15] Recent investigations highlight that the synergistic interplay between solvents and diluents, mediated by intermolecular forces (hydrogen bonding, dipole interactions, etc.), can dynamically reshape the solvent geometry and coordination activity. This adaptive conformational change offers a direct handle for programming anion-involved solvation architectures.[16,17] Nevertheless, the efficacy of the aforementioned strategies is fundamentally

Received: February 9, 2026
Revised: April 18, 2026
Accepted: April 23, 2026
Published: April 30, 2026

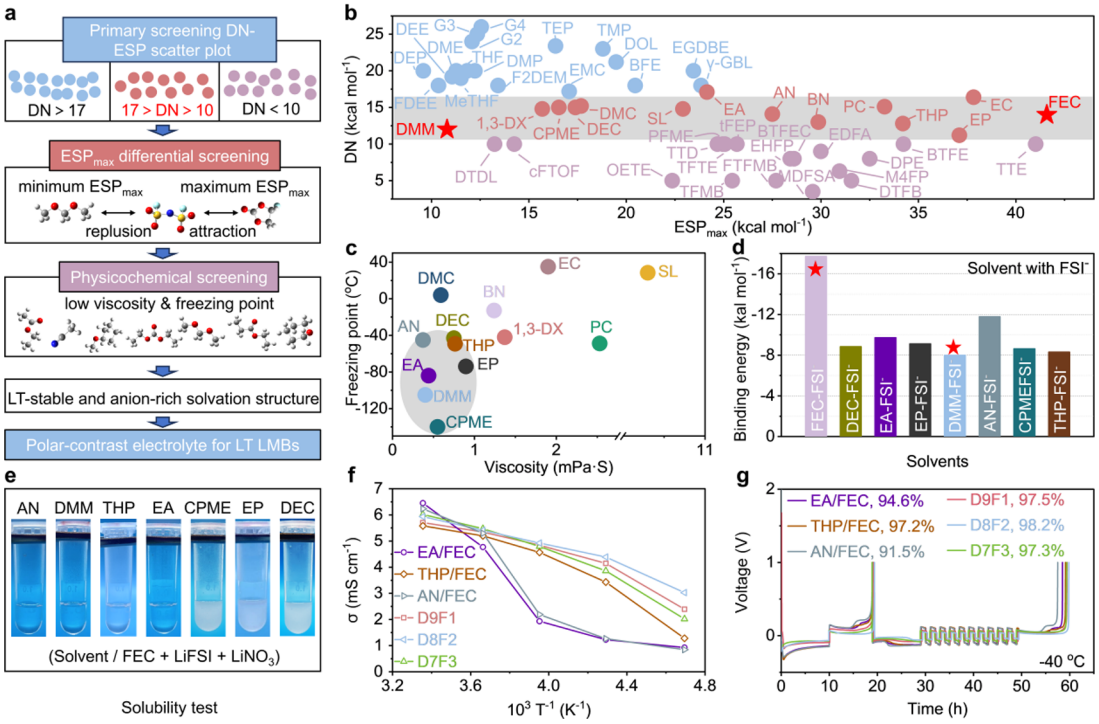

Figure 1. Design strategy and screening principle for potential solvents. (a) Schematic illustration of electrolyte design strategy. (b) Plot of ESP_{max} and DN of common ether, ester, and nitrile solvents. (c) The map of freezing point and viscosity of solvents. (d) The binding energies between solvents and FSI^-. (e) Solubility tests for different electrolytes. (f) Ionic conductivities of different electrolytes from 25 to −60 °C. (g) Aurbach CE tests of Li|Cu asymmetrical cells employing different electrolytes at −40 °C.

constrained under LT conditions. As temperature decreases, the thermal motion of solvents diminishes, and the coordination with Li^+ strengthens, causing anions to be expelled from the solvation sheath.[18,19] This leads to a sharp decline in ion transport efficiency, a surge in interfacial charge transfer impedance, and exacerbated side reactions.[20,21] Therefore, there is a pressing need to develop novel electrolyte design strategies toward durable, anion-involved solvation structures capable of withstanding LT conditions.

Herein, by systematically regulating the interactions between solvents and FSI^-, we screened polar-contrast solvent pairs (fluoroethylene carbonate (FEC) and dimethoxymethane (DMM)) for electrolyte engineering to establish LT-stable and FSI^--rich solvation structures. The primary solvent DMM with the lowest maximum electrostatic potential (ESP_{max}) displays a weakened DMM−FSI^- interaction at LTs, promoting the entry of FSI^- into the solvation shell. The coordinated FEC cosolvent with higher ESP_{max} exhibits strong ion−dipole interactions with the FSI^- anion at LTs, which anchors more FSI^- into the solvation sheath of Li^+. Such an FSI^--dominated solvation structure induces the formation of fluorine-rich solid electrolyte interphase (SEI), leading to uniform Li deposition under LT conditions. Furthermore, the enhanced dipole−dipole interactions of DMM and FEC accelerate the desolvation process, significantly enhancing interfacial dynamics. As a result, the designed electrolyte achieves a high Li metal Coulombic efficiency (CE) of 99.2% at 25 °C and maintains 98.2% even at −40 °C. The electrolyte is also applied in Li|SPAN full cells with a practical cathode loading of 4.5 mAh cm^{-2}, retaining 80% and 55% of its room temperature capacity when charged and discharged at −40 and −60 °C, respectively. The practical viability is further demonstrated by Ah-level Li metal pouch cells completing 50 cycles at −20 °C, with exceptional capacity−temperature−lifespan balance, surpassing the most reported LT LMBs. This work establishes a general electrolyte design paradigm for constructing LT-stable and anion-dominated solvation structures, providing new insights into cryogenic LMBs.

RESULTS AND DISCUSSION

Solvents Screening Based on Anion−Dipole Interactions

The stability of electrolytes is fundamentally governed by the energetics of intermolecular interactions, wherein ion−solvent and solvent−solvent interactions dictate bulk transport kinetics and interfacial stability.[16] To address the stringent requirements of LT LMBs, over 70 solvents with diverse chemical structures, including ethers, esters, and nitriles, were screened using a multidimensional strategy to elucidate their structure−property relationships (Figure 1a). Given the ambiguous physical interpretation of conventional polarity descriptors, donor number (DN) serves as a more reliable descriptor for quantifying the coordination ability of solvents toward Li^+.[22] Solvents with moderate DN values were first selected to maintain balanced ion dissociation-transport behavior, avoiding excessively strong or weak solvent−Li^+ interactions (Figure 1b and Table S1). To further evaluate the anion−solvent interaction, ESP_{max} was employed as a key descriptor. Among them, FEC exhibits the highest ESP_{max}, while DMM displays the lowest ESP_{max}, indicating a pronounced contrast in the interaction with anions. In parallel, solvents with low freezing points and low viscosities were identified to ensure favorable transport properties under LT conditions (Figure 1c and Table S2). Subsequently, the binding energies between the solvents and FSI^- were calculated. As depicted in Figure 1d and Figure S1, FEC-FSI^- exhibits the highest binding energy, while

https://doi.org/10.1021/jacs.6c03001
J. Am. Chem. Soc. 2026, 148, 19128−19137

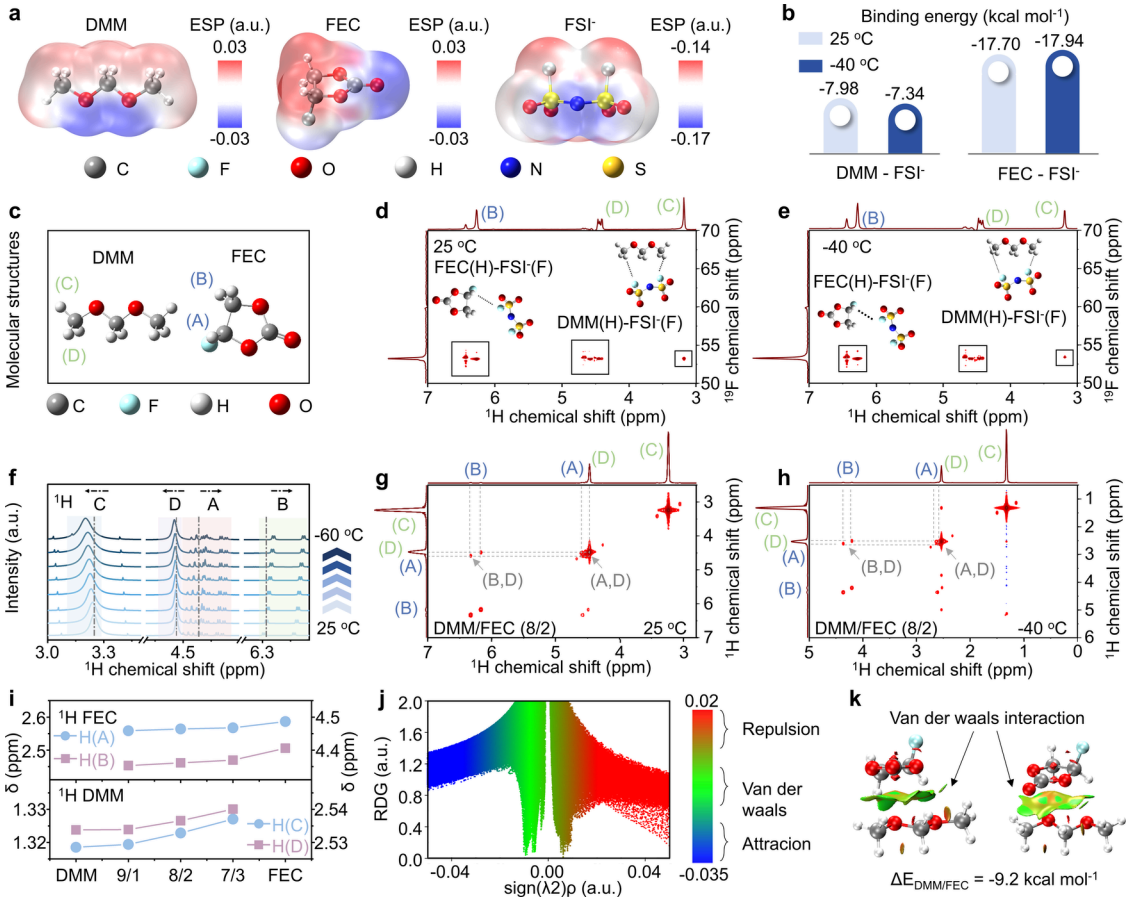

Figure 2. Exploration of the ion−dipole and dipole−dipole interactions. (a) ESP maps of solvents and FSI^-. (b) Binding energies of DMM/FEC and FSI^- at different temperatures. (c) Schematic diagram depicting the molecular architecture, with labels A−D denoting the positions of H atoms within molecules. $^1H-^{19}F$ HOESY NMR spectra of D8F2 at (d) 25 and (e) −40 °C. (f) ^1H NMR spectra of DMM/FEC (8/2) at different temperatures. $^1H-^1H$ COSY NMR spectra of DMM/FEC (8/2) at (g) 25 °C and (h) −40 °C. (i) ^1H NMR spectra of solvent mixtures with different ratios. (j) Scatter plot and (k) gradient isosurface plot of DMM/FEC by the RDG method.

DMM-FSI^- shows the lowest. The energy disparity arising from the polarity contrast enables multiscale modulation of the FSI^- coordination behavior. Accordingly, DMM was chosen as the primary solvent to suppress excessive anion constraint in the bulk electrolytes, while FEC was introduced as the cosolvent to modulate FSI^- coordination behavior via its stronger binding affinity with the anion. Meanwhile, the strong dipole−dipole interactions between DMM and FEC enhance intermolecular synergistic effects under LT conditions (Figures S2 and S3). Furthermore, different electrolytes were prepared by mixing various primary solvents with FEC cosolvent. Li salt solubility tests reveal that only a few electrolytes form homogeneous and stable dissolution systems, including AN/FEC, DMM/FEC, THP/FEC, and EA/FEC (Figure 1e). Among these, D8F2 (DMM/FEC = 8:2 by volume) exhibits the highest ionic conductivity across the entire temperature range (Figure 1f and Figure S4). In addition, the Li plating/stripping efficiency of different electrolytes was evaluated via Aurbach CE tests at −40 °C. Figure 1g shows that D8F2 retains a high efficiency of 98.2% at −40 °C, significantly outperforming the comparative electrolytes. Based on these results, the DMM/FEC solvent pair is selected for electrolyte engineering in LT LMBs.

Temperature-Dependent Ion−Dipole and Dipole−Dipole Interactions

To elucidate the solvation structure evolution of D8F2 across temperatures, the interaction differences between DMM/FEC and FSI^- were investigated. As shown in Figure 2a, the ESP distribution of FEC reveals that regions with a higher positive potential are concentrated on H atoms, while the positive potential on H atoms in DMM is significantly weakened. This difference directly leads to a significant difference in the interaction strength between the DMM/FEC solvents and FSI^-. At 25 °C, the binding energy of FEC-FSI^- is −17.70 kcal mol^{-1}, substantially stronger than that of DMM-FSI^- (−7.98 kcal mol^{-1}). At −40 °C, the binding energy of FEC-FSI^- further increases to −17.94 kcal mol^{-1}, while that of DMM-FSI^- decreases to −7.34 kcal mol^{-1} (Figure 2b and Figure S5). The evolution of binding energy promotes FSI^- entry into the Li^+ solvation shell under LT conditions. 2D $^1H-^{19}F$ heteronuclear Overhauser enhancement spectroscopy (HOESY) was conducted to probe the anion−solvent interaction at the molecular level. At 25 °C, the distinct correlation between FEC(H)-FSI^-(F) and DMM(H)-FSI^-(F) indicates an electrostatic interaction between solvents and FSI^- in D8F2 (Figure 2c,d). As temperature decreases (−40 °C), the intensity of the DMM(H)-FSI^-(F) cross-peak (peak H(C)) attenuates, whereas the FEC(H)-FSI^-(F) peak (peak H(B)) enhances (Figure 2e). This suggests a temperature-

https://doi.org/10.1021/jacs.6c03001
J. Am. Chem. Soc. 2026, 148, 19128−19137

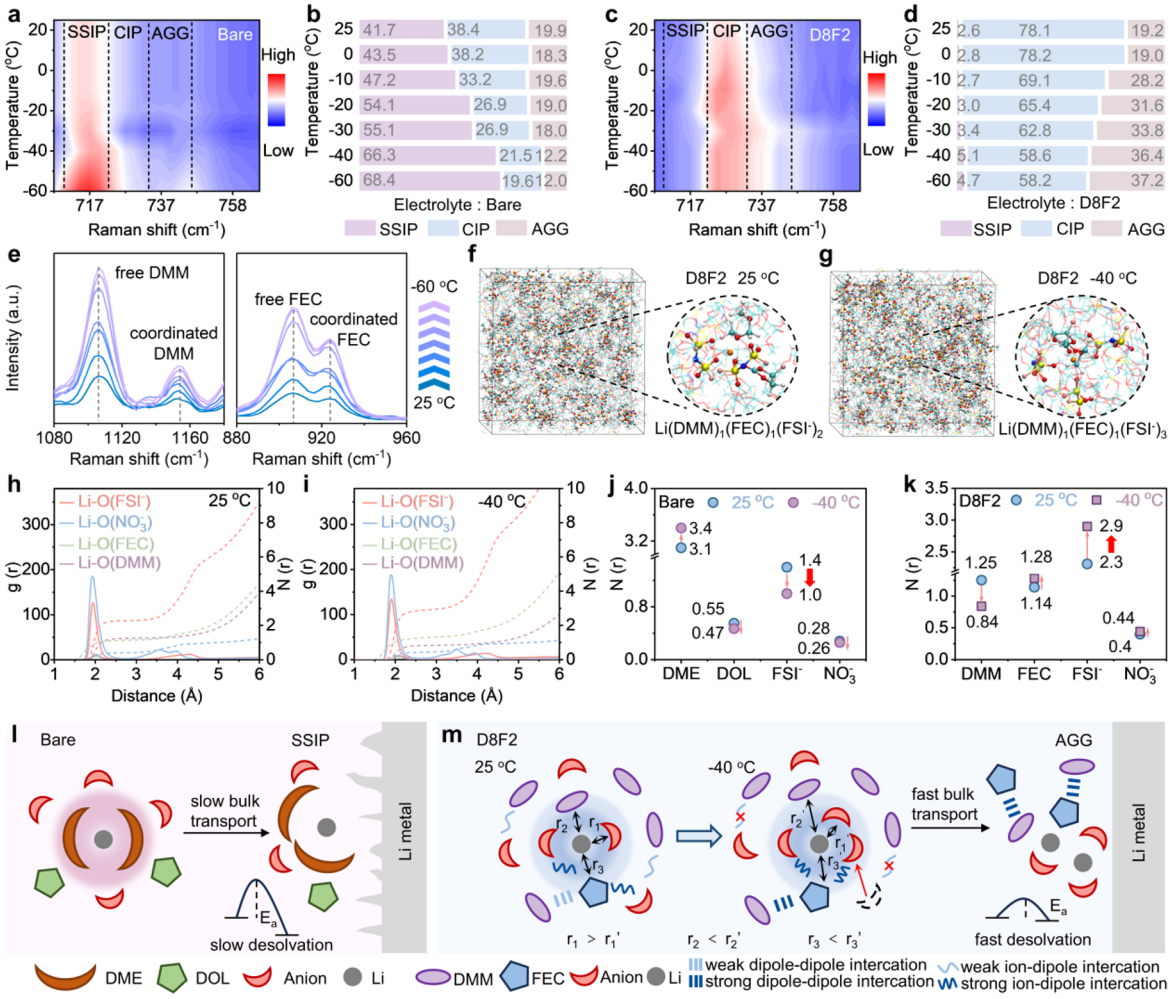

Figure 3. Evolution behaviors of solvation structures. Variable-temperature Raman spectra of the S−N−S bending vibrational mode of FSI^- in (a) Bare and (c) D8F2. Percentage of SSIPs/CIPs/AGGs of (b) Bare and (d) D8F2 obtained by Raman spectra. (e) Variable-temperature Raman spectra of DMM and FEC molecules in D8F2. 3D snapshots of D8F2 collected at (f) 25 °C and (g) −40 °C obtained by MD simulation. RDF and CN plots of D8F2 (h) at 25 °C and (i) −40 °C. (j) Average CN of Li^+-O(DME), Li^+-O(DOL), Li^+-O(FSI^-), and Li^+-O(NO_3^-) at 25 and −40 °C. (k) Average CN of Li^+-O(DMM), Li^+-O(FEC), Li^+-O(FSI^-), and Li^+-O(NO_3^-) at 25 and −40 °C. Schematic illustration of the solvation transition mechanisms in (l) Bare and (m) D8F2 under different temperatures.

induced modulation of intermolecular interaction, indicating a strengthened FEC-FSI^- binding affinity and diminished DMM-FSI^- association, leading to FSI^--dominated solvation structures at LTs.

The temperature-dependent behavior of DMM and FEC dipole−dipole interactions was also investigated. ^{1}H NMR spectra spanning 25 °C to −60 °C display broadened peak widths, consistent with strengthened intermolecular association (Figure 2f).[23,24] Two-dimensional (2D) ^{1}H−^{1}H correlation spectroscopy (COSY) was employed to reveal the proton coupling between various molecules. At 25 °C, H atoms at the A and B sites in FEC interact with the H atom at the D site in DMM, resulting in a strong and directional coupling effect (Figure 2g). This coupling interaction persists at −40 °C, with cross-peak intensity rising as the FEC amount escalates, signifying enhanced spatial proximity of these proton bonds and strengthened interplay (Figure 2h and Figure S6). The concentration-dependent ^{1}H NMR chemical shift changes observed in the DMM/FEC mixtures indicate progressively strengthened dipole−dipole interactions between DMM and FEC as the FEC content increases (Figure 2i and Figure S7). The strength and spatial distribution of dipole−dipole interactions between DMM and FEC were further analyzed using the reduced density gradient (RDG) method. Figure 2j depicts green peaks at −0.02 to 0.00 au of the $(\lambda_2)\rho$ symbol, indicating a dipole−dipole interactions within DMM and FEC. This interaction originates from the carbon ring of FEC and the O atom of DMM, as visualized by the gradient isosurface plot (Figure 2k). Between two molecules, the RDG isosurface colors greenish-orange correspond to van der Waals interaction. The strong interactions between DMM and FEC accelerate the desolvation process, thereby enhancing interfacial dynamics at LTs.

Temperature-Dependent Solvation Structure Evolution Behaviors

The intermolecular interactions between DMM/FEC and FSI^- exert a profound regulatory influence on solvation structures, dictating the dynamic evolution of FSI^--dominated configurations. The downfield shift in ^{7}Li spectra with increasing FEC amount indicates that the synergistic interaction between FEC and DMM weakens the coordination strength of the Li^+ solvation sheath, while the upfield shift in the ^{19}F spectra of FSI^- offers evidence for the enhanced coordination of Li^+ with

https://doi.org/10.1021/jacs.6c03001
J. Am. Chem. Soc. 2026, 148, 19128−19137

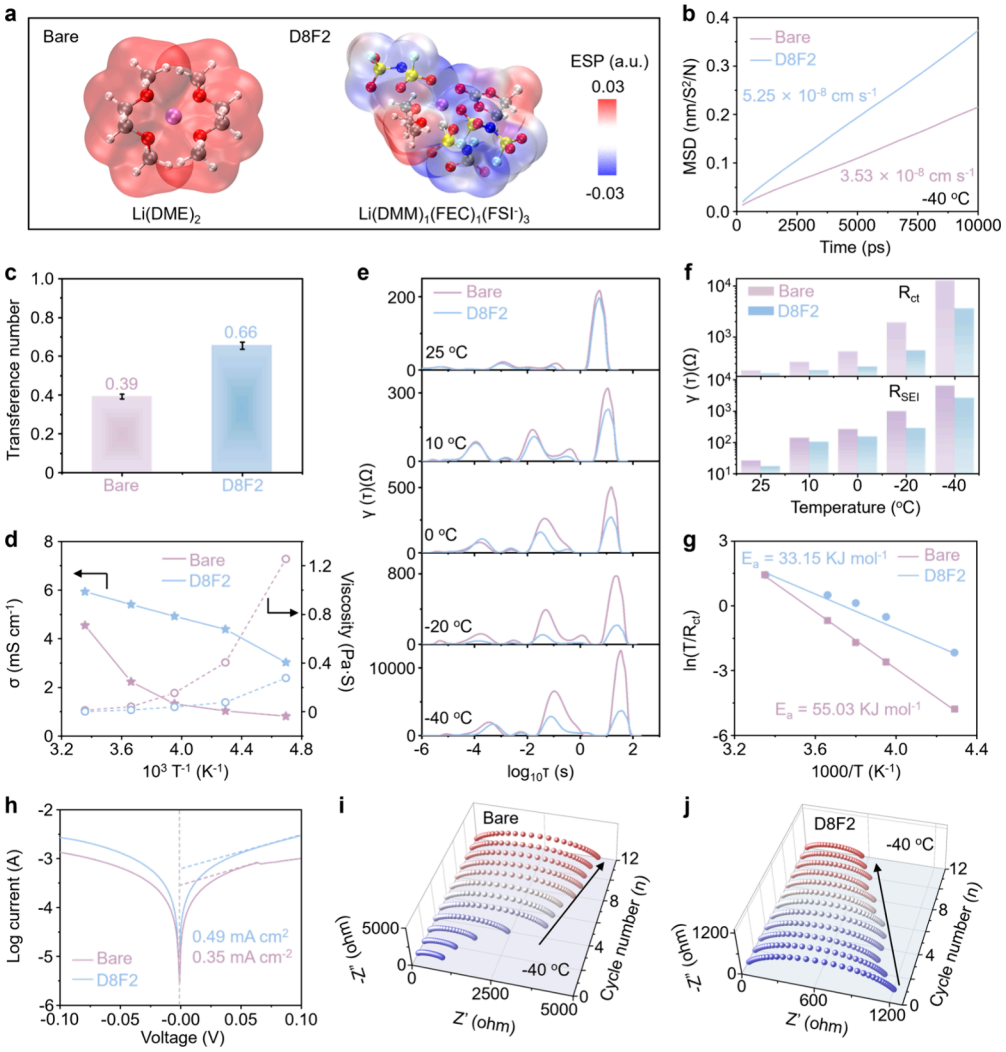

Figure 4. Kinetic performance evaluation at LTs. (a) ESP mapping of $Li(DME)_2$ and $Li(DMM)_1(FEC)_1(FSI^-)_3$ solvation structure in Bare and D8F2. (b) MSD curves of Li^+ in Bare and D8F2 at −40 °C. (c) Li^+ transference numbers of Bare and D8F2. (d) Temperature-dependent conductivity and viscosity of Bare and D8F2. (e) DRT profiles from EIS measurements between 25 °C and −40 °C. (f) Summary of peak maxima as a function of temperature in Bare and D8F2 for SEI and charge transfer peaks. (g) Activation energy calculations and comparisons. (h) Exchange current densities tested by Li||Li symmetric cells. In situ EIS curves of Li||Li symmetric cells during charge/discharge process in (i) Bare and (j) D8F2 at −40 °C.

FSI^- (Figure S8). To investigate the solvation evolution of electrolytes across varying temperatures, Raman spectra were collected. The S−N−S bending vibrational mode of FSI^- within the 700−780 cm^{-1} range was probed to elucidate the FSI^- coordination behavior (Figures S9 and S10). Specifically, the Raman bands at 719, 730, and 745 cm^{-1} correspond to distinct coordination states of FSI^-, assigned to solvent-separated ion pairs (SSIPs), contact ion pairs (CIPs), and ion aggregates (AGGs), respectively. With declining temperature, the proportion of SSIP configurations increases in Bare, signifying a solvent-dominant solvation transition at LTs driven by the progressively strengthening Li^+-solvent interaction (Figure 3a,b). Conversely, the solvation structure of D8F2 displays an increased prevalence of CIP and AGG configurations at LTs, attributing to ion−dipole interactions between FEC/DMM and FSI^- (Figure 3c,d). The solvation structure is further consolidated in Figure 3e. Upon cooling, the signal of free DMM strengthens, while that of coordinated DMM stays comparatively weak, corresponding to the gradual removal of DMM from the Li^+ solvation shell. Simultaneously, the intensity of coordinated FEC rises markedly, indicating enhanced Li^+-FEC coordination under LT conditions. At LTs, free DMM exhibits weakened interactions with FSI^-, facilitating the initial entry of anions into the solvation shell. Complementarily, the coordinated FEC cosolvent engages in strong interactions with FSI^-, which further anchors these anions within the Li^+ solvation sheath, collectively establishing an FSI^--enriched coordination environment.

Molecular dynamics (MD) simulations were conducted to explore Li^+ solvation structures across varying temperatures. The snapshots of Bare are shown in Figure S11. Radial distribution functions (RDF) are constructed to analyze the solvent and anion species surrounding Li^+. In Bare, the coordination numbers (CNs) of Li^+-O(DME), Li^+-O(DOL), Li^+-O(FSI^-), and Li^+-O(NO_3^-) are 3.1, 0.55, 1.4, and 0.28, respectively, forming the solvent-dominated solvation structure of $Li^+(DME)_{3.1}(DOL)_{0.55}(FSI^-)_{1.4}(NO_3^-)_{0.28}$ at 25 °C (Figure S12a and Tables S3 and S4). As the temperature drops to −40 °C, the CN of Li^+-O(DME) increases while the CNs of Li^+-O(FSI^-) and Li^+-O(NO_3^-) decrease, owing to the enhanced

https://doi.org/10.1021/jacs.6c03001
J. Am. Chem. Soc. 2026, 148, 19128−19137

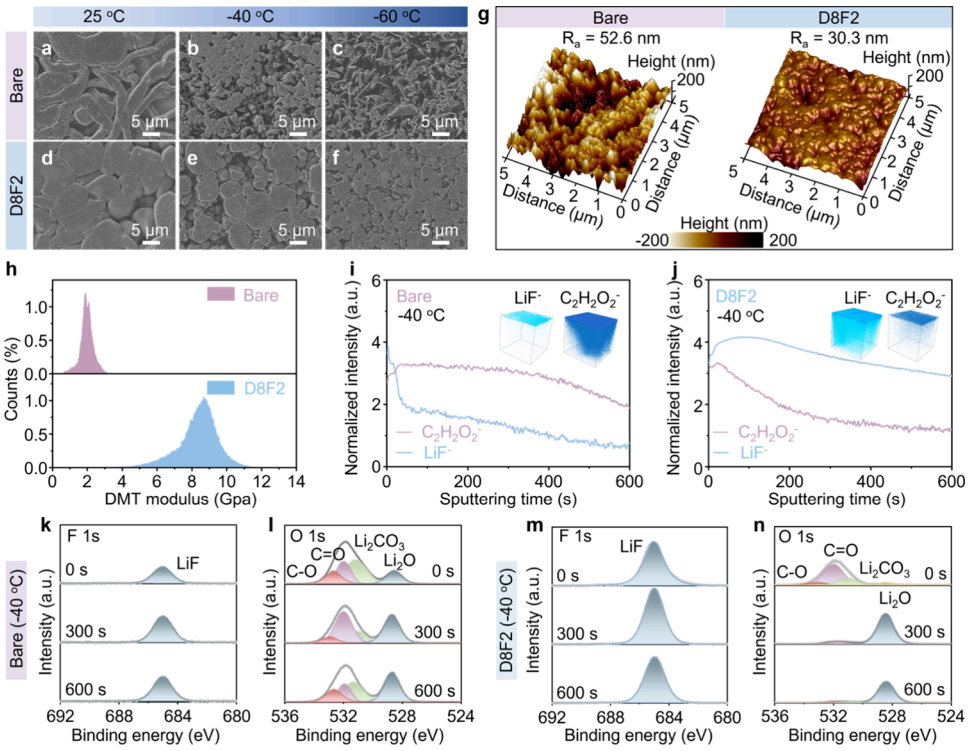

Figure 5. Li deposition morphology and interface chemistry at LTs. SEM images of Li deposition in Bare at (a) 25 °C, (b) −40 °C, and (c) −60 °C. SEM images of Li deposition in D8F2 at (d) 25 °C, (e) −40 °C, and (f) −60 °C. (g) AFM morphology of Li deposition in Bare and D8F2 at −40 °C. (h) DMT modulus distribution of SEI in Bare and D8F2 at −40 °C. TOF-SIMS depth profiles for LiF^- and $C_2H_2O_2^-$ on Li metal anode in (i) Bare and (j) D8F2 at −40 °C. Insets: TOF-SIMS 3D reconstruction of LiF^- and $C_2H_2O_2^-$. (k) F 1s and (l) XPS spectra of the SEI derived from Bare at −40 °C. (m) F 1s and (n) O 1s XPS spectra of SEI derived from D8F2 at −40 °C.

polarity of solvent molecules at LTs (Figure 3j and Figure S12b). In contrast, D8F2 exhibits an anion-dominated solvation structure at both 25 and −40 °C (Figure 3f,g). The CNs of Li^+-O(DMM), Li^+-O(FEC), Li^+-O(FSI^-), and Li^+-O(NO_3^-) are 1.25, 1.14, 2.3, and 0.4, respectively, yielding the FSI^--dominated solvation structure of $Li^+(DMM)_{1.25}(FEC)_{1.14}(FSI^-)_{2.3}(NO_3^-)_{0.4}$ at 25 °C (Figure 3h and Table S5). As the temperature decreases, the CN of FEC rises, whereas that of DMM falls (Figure 3i,k). This observation is consistent with the results of the Raman spectra. Dynamic reorganization of the Li^+ solvation environment emerges from cooperative interactions between DMM/FEC and FSI^-. Meanwhile, DMM in the bulk electrolyte, through the dipole−dipole interaction with FEC, drives FEC away from Li^+, thereby enabling the competitive coordination of FSI^- at LTs (Table S6). The dynamic evolution of solvation structures in different electrolytes at different temperatures is presented in Figure 3l,m. Bare displays the solvent-dominated solvation structure, which leads to severe solvent decomposition and Li dendrite formation. Moreover, the strong Coulombic interaction between DME and Li^+ exacerbates the kinetic barrier of desolvation process under LTs. By contrast, in D8F2, the enhanced ion−dipole interaction between coordinated FEC and FSI^- anchors more FSI^- within the Li^+ solvation sheath. The weak DMM−FSI^- interaction allows FSI^- to break free from the confinement of DMM, promoting the formation of the AGG structures. Such a FSI^--dominated solvation structure not only improves ionic transport efficiency but also induces the formation of a fluorine-rich SEI, which accelerates the desolvation process and induces uniform Li deposition at LTs.

Kinetic Behavior of Electrolytes at LTs

The representative solvation structures were selected for ESP calculations. At equivalent energy scales, the Li-$(DMM)_1(FEC)_1(FSI^-)_3$ configuration of D8F2 exhibits significantly reduced electrostatic potential compared to $Li(DME)_2$ structure in Bare, demonstrating suppressed electrostatic repulsion that facilitates Li^+ migration (Figure 4a).[25] The mean square displacement (MSD) of Li^+ ions was computed at −40 and 25 °C, revealing substantially improved diffusion coefficients in D8F2 relative to Bare (Figure 4b and Figure S13). Furthermore, D8F2 achieves an exceptional Li^+ transference number of 0.66, much higher than that of Bare (0.38) (Figure 4c and Figure S14). To minimize the contributions of cation−anion interactions, the Li^+ transference number was evaluated by combining the total ionic conductivity measured by impedance spectroscopy and anion mobility determined by DOSY NMR spectroscopy (Figures S15 and S16).[26] Differential scanning calorimetry (DSC) curves reveal that D8F2 exhibits a significantly lower freezing point compared to Bare (Figure S17), indicating enhanced resistance to solidification at LTs. Temperature-dependent ionic conductivity and viscosity further highlight the transport advantages of D8F2 (Figure 4d and Figure S18). Across the entire temperature range, D8F2 delivers a higher ionic conductivity and lower viscosity than Bare. Notably, at −60 °C, D8F2 maintains a conductivity of 3 mS cm^{-1}, whereas that of Bare drops below 0.8 mS cm^{-1}. The reduced viscosity and enhanced conductivity in D8F2 effectively mitigate the sluggish ion transport encountered under LT conditions, in good agreement with the enhanced Li^+ diffusion and transference behavior discussed above.

https://doi.org/10.1021/jacs.6c03001
J. Am. Chem. Soc. 2026, 148, 19128−19137

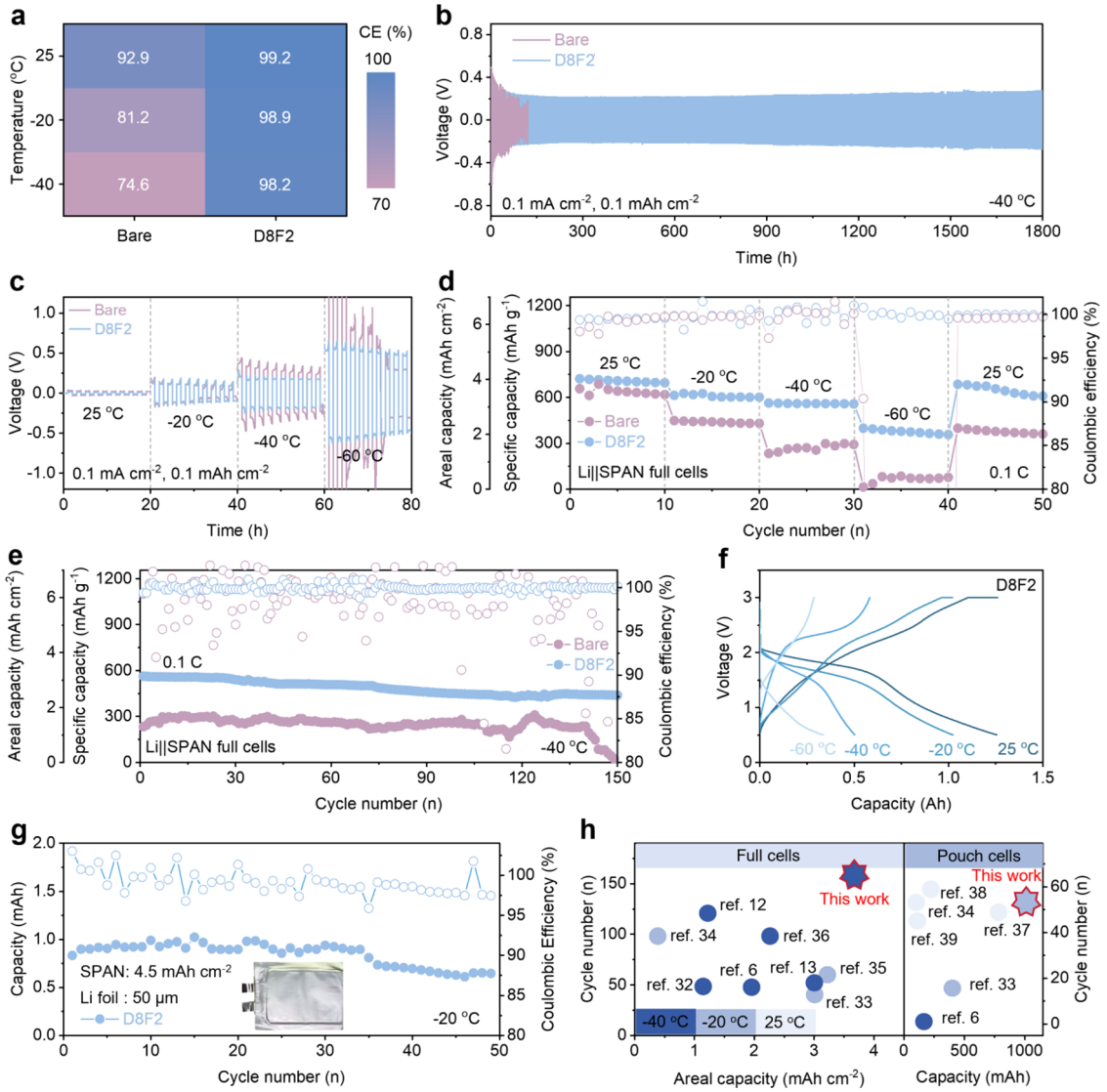

Figure 6. Electrochemical performance of LMBs under cryogenic conditions. (a) Heatmaps indicating the CE values under different temperatures. (b) Cycling performance of Li||Li symmetric cells with different electrolytes at −40 °C. (c) Temperature-dependent cycling of Li||Li symmetric cells with different electrolytes. (d) Variable-temperature cycling of Li||SPAN full cells with different electrolytes. (e) Cycling performance of Li|| SPAN full cells with different electrolytes at −40 °C. (f) Voltage profiles of the Li||SPAN pouch cells with D8F2 at different temperatures. (g) Cycling performance of 1Ah Li (50 μm)||SPAN (4.5 mAh cm^{-2}) pouch cells with D8F2 at −20 °C. (h) Comparison of LT cycling performance of LMBs with D8F2 and previous reports.[6,12,13,32−39]

The impact of dipole interactions in D8F2 on Li^+ interfacial kinetics was corroborated through distribution of relaxation times (DRT) analysis. This analysis classified different electrochemical processes through their local maxima in a continuous distribution function (Figure S19).[27] The charge transfer resistance (R_{ct}), which manifests in the low-frequency regime ($10^{-1} < \tau < 10^{2}$), reflects the faradaic reaction kinetics associated with Li^+ desolvation process. The intermediate-frequency peak ($10^{-3} < \tau < 10^{-1}$) is associated with Li^+ diffusion across the SEI.[28,29] Both R_{ct} and R_{SEI} exhibit pronounced temperature-dependent behavior (Figure 4e). Specifically, D8F2 maintains consistently lower R_{ct} and R_{SEI} values across a temperature range from 25 to −40 °C (Figure 4f). These values are substantially lower than those of Bare, highlighting the superior charge transfer capabilities of D8F2. The activation energy for the Li^+ desolvation process was calculated to be 33.15 and 55.03 kJ mol^{-1} in D8F2 and Bare, respectively, well supporting the DRT results (Figure 4g and Figure S20). The enhanced LT deposition kinetics in D8F2 were further verified by the exchange current density derived from the Tafel plots. As displayed in Figure 4h, D8F2 achieves an exchange current density of 0.49 mA cm^{-2}, significantly higher than that of Bare (0.35 mA cm^{-2}), indicating markedly enhanced charge transfer kinetics. This advantage persists at LTs, with D8F2 exhibiting 0.05 mA cm^{-2} and 3.98 μA cm^{-2} at −20 and −40 °C, respectively, whereas Bare exhibits only 0.01 mA cm^{-2} and 1.16 μA cm^{-2} under identical conditions (Figure S21). Furthermore, in situ EIS spectra were tested to visually reflect the kinetic behavior of different electrolytes at −40 °C. As shown in Figure 4i and Figure S22a, Bare manifests progressively rising impedance and fluctuating plating/stripping profiles during the cycling process, stemming from byproducts and dead Li formation and sluggish charge transfer kinetics at LTs. Conversely, D8F2 demonstrates a gradually diminishing impedance throughout cycling, indicative of

https://doi.org/10.1021/jacs.6c03001
J. Am. Chem. Soc. 2026, 148, 19128−19137

superior electrochemical kinetics under cold conditions (Figure 4j and Figure S22b).

Li Morphology and Interface Chemistry at LTs

The morphology of Li deposition was characterized by field emission scanning electron microscopy (FE-SEM) at different temperatures. Li morphology in Bare manifests a nodule-like shape with rounded edges/corners, along with a scattering of dendrites (Figure 5a). A key morphological evolution induced by decreasing the temperature is the progressive size reduction and concomitant sharpening of these dendritic features (Figure 5b,c). However, D8F2 consistently reveals a dense and dendrite-free structure across the investigated temperatures (25 °C, −40 °C, and −60 °C) (Figure 5d−f). This uniform Li deposition morphology is attributed to the fast interfacial reaction kinetics and fluorine-rich SEI at LTs. The atomic force microscopy (AFM) was used to evaluate the surface roughness and mechanical properties of Li deposition. Figure 5g displays the height images of Li deposition in Bare and D8F2. The Li deposition in D8F2 demonstrates an average roughness of 30.3 nm, considerably lower than that in Bare (52.6 nm), indicating the homogeneity of SEI and Li deposition in D8F2. Additionally, the average Derjaguin−Muller−Toporov (DMT) modulus of the SEI in D8F2 reaches 8.7 GPa, which is 4.5 times higher than that in Bare (1.9 GPa) (Figure 5h). The enhanced mechanical properties of SEI in D8F2 can well tolerate large volume fluctuations for Li plating/stripping, promoting a uniform Li deposition at LTs.

Time-of-flight secondary ion mass spectrometry (TOF-SIMS) analysis of SEI chemical compositions across room and low temperatures revealed a comprehensive spatial distribution and relative intensities of inorganic/organic species. From the depth profiles and the corresponding three-dimensional distribution (Figure S23a), organic fragments ($C_2H_2O_2^-$) constitute the predominant component in the SEI of Bare, whereas LiF^- exhibit significantly lower abundance at 25 °C. This compositional disparity is maintained at LTs (Figure 5i). In contrast, the D8F2-derived SEI exhibits an organic outer layer and a fluorine-rich inner structure (Figure S23b and Figure 5j). Despite an initial rise and subsequent decline with sputtering depth, LiF^- remains dominant at both 25 °C and −40 °C. The fluorine-rich inner layer generates numerous phase boundaries and vacancies, which facilitate Li^+ diffusion through reduced energy barriers and enhanced surface energy, effectively inhibiting the Li dendrite formation.[30] To further probe the chemical composition of the SEI, depth-resolved X-ray photoelectron spectroscopy (XPS) with Ar^+ sputtering was conducted at different temperatures. In the F 1s spectra, the peak at a binding energy of 684.98 eV associates with Li−F. D8F2 demonstrates depth-dependent Li−F enrichment in SEI layers at both 25 and −40 °C, while Bare maintains consistently low Li−F concentrations throughout the depth profile (Figure 5k,m and Figure S24). The O 1s spectra exhibit indications of C−O, C=O, Li_2CO_3, and Li_2O bonds at 532.7 531.95, 531.2, and 528.55 eV, respectively. Figure 5l and Figure S25a demonstrate significant organic component accumulation (C−O and C=O) throughout the sputtered region of Bare, with particularly pronounced organic enrichment at LTs due to exacerbated solvent decomposition. As evidenced by Figure 5n and Figure S25b, organic SEI components derived from D8F2 remain confined to the surface region across, coupled with prominent Li_2O species formation. Overall, the fluorine-rich SEI formed in D8F2 provides highly conductive ion transport pathways and effectively suppresses Li dendrite proliferation, thereby stabilizing the interfacial behavior under LT conditions. This SEI chemistry originates from the LT-stable and FSI^--rich solvation structure in D8F2, which exhibits a higher reduction propensity and preferentially drives the formation of a LiF-rich interphase.

Electrochemical Performance of Half Cells and Full Cells at LTs

Subsequently, we investigated the electrochemical performance of the Li metal at LTs. The CE values of Li||Cu asymmetrical cells are collected under different temperatures. As shown in Figure 6a and Figure S26, the CEs of Bare deteriorate markedly with decreasing temperature, declining from 92.9% at 25 °C to 81.2% at −20 °C and further to 74.6% at −40 °C. In contrast, D8F2 maintains a high CE of 99.2% at 25 °C, 98.9% at −20 °C, and 98.2% at −40 °C, demonstrating excellent Li plating/stripping reversibility at LTs, attributed to good interfacial transport kinetics.[1] Li||Li symmetric cells with D8F2 have steady cyclability over 6400 h at 25 °C, whereas that of Bare displays a continuously increasing voltage polarization (Figure S27). When the temperature drops to −40 °C, the cells using Bare exhibit short circuit after 140 h, while the cells with D8F2 stably cycle for over 1800 h (Figure 6b). Since overpotential is the critical parameter in LMBs as it is directly related to the energy efficiency,[31] we evaluated this parameter by cycling Li||Li symmetric cells under various temperatures. As shown in Figure 6c, the cells with Bare exhibit a rapid increase in polarization as the temperature decreases. Benefiting from enhanced electrochemical kinetics and stable SEI, symmetrical cells employing D8F2 sustain consistently lower overpotentials from 25 °C to −60 °C compared to that with Bare.

To evaluate the LT performance of D8F2, Li||SPAN full cells were assembled with an industrial high-loading SPAN cathode (4.5 mAh cm^{-2}). The full cells with Bare exhibit rapid capacity decay, retaining only 28% of their initial capacity after 150 cycles at 25 °C due to severe polysulfide shuttling (Figure S28). In contrast, full cells with D8F2 yield a specific capacity of 720 mAh g^{-1} and maintain 70% capacity retention over 150 cycles owing to suppressed polysulfide dissolution, substantially outperforming those with D9F1 (714 mAh g^{-1}, 50%) and D7F3 (690 mAh g^{-1}, 47%) (Figure S29). As shown in Figure 6d and Figure S30, full cells employing D8F2 deliver specific capacities of 708 mAh g^{-1}, 626 mAh g^{-1}, 560 mAh g^{-1}, and 390 mAh g^{-1} when both charged and discharged at 25, −20, −40, and −60 °C, respectively. In the case of Bare, dramatically reduced capacities can be observed, with low specific capacities of 656 mAh g^{-1}, 449 mAh g^{-1}, 242 mAh g^{-1}, and 83 mAh g^{-1}, respectively. Additionally, the cycling performance of Li||SPAN full cells was conducted at −40 °C. The full cells with D8F2 deliver a decent initial capacity of 563 mAh g^{-1} with 80% of capacity retention after 150 cycles with an average CE of 99.5% (Figure 6e and Figure S31). In contrast, full cells with Bare deliver a low initial capacity of only 300 mAh g^{-1} and undergo a rapid capacity decay after 150 cycles. To further examine the potential of D8F2 toward practical LMBs at LTs, Ah-level Li||SPAN pouch cells were fabricated. As shown in Figure 6f, the pouch cells deliver capacity of 1.02, 0.51, and 0.34 Ah at −20 °C, −40 °C, and −60 °C, respectively, corresponding to capacity retention of 82%, 41%, and 27% relative to 25 °C. As shown in Figure 6g,

https://doi.org/10.1021/jacs.6c03001
J. Am. Chem. Soc. 2026, 148, 19128−19137

the pouch cell with D8F2 delivers a reversible capacity of 0.8 Ah, which is charged and discharged at −20 °C, maintaining high reversibility over 50 cycles (Figure S32). Comparative analysis with existing literature indicates that our designed electrolyte offers advantages in terms of areal capacity and cycle life at LTs in full cells (Figure 6h and Table S7). Remarkably, our Ah-level Li||SPAN pouch cells demonstrate exceptional cycling stability and capacity retention at LTs compared with other reports (Table S8).

CONCLUSIONS

In summary, we propose a polarity-contrast electrolyte design strategy that stabilizes FSI^--dominated solvation structure under LT conditions by delicately regulating solvent−FSI^- interactions. Employing the DMM/FEC solvent pair, weakened DMM−FSI^- interaction at LTs facilitates the FSI^- coordination, while the strengthened FEC−FSI^- interaction further anchors FSI^- within solvation structures. This cooperative solvation regulation preserves FSI^--dominated solvation environment upon cooling, leading to accelerated interfacial kinetics and the formation of a fluorine-rich SEI. Consequently, uniform Li deposition and highly reversible Li plating/stripping are achieved from 25 to −60 °C. The Li|| SPAN full cells exhibit a high areal capacity and excellent LT cycling stability. The practical viability is further demonstrated by Ah-level Li metal pouch cells with enhanced cycle life. This work establishes a general electrolyte design paradigm for constructing LT-resilient and anion-rich solvation structures, offering new insights into advanced LT LMBs.

ASSOCIATED CONTENT

Supporting Information

The Supporting Information is available free of charge at https://pubs.acs.org/doi/10.1021/jacs.6c03001.

Experimental details, additional characterizations (SEM, NMR, Raman, etc.), additional electrochemical tests, and supplementary tables and notes (PDF)

AUTHOR INFORMATION

Corresponding Authors

Dongdong Wang − *Power Battery & Systems Research Center, State Key Laboratory of Catalysis, Dalian Institute of Chemical Physics, Chinese Academy of Sciences, Dalian 116023, China*; orcid.org/0000-0002-0391-8242; Email: dongdongwang@dicp.ac.cn

Xinli Guo − *State Key Laboratory of Engineering Materials for Major Infrastructure, School of Materials Science and Engineering, Southeast University, Nanjing 211189, China*; Email: guo.xinli@seu.edu.cn

Dan Luo − *Power Battery & Systems Research Center, State Key Laboratory of Catalysis, Dalian Institute of Chemical Physics, Chinese Academy of Sciences, Dalian 116023, China*; Email: luodan@dicp.ac.cn

Zhongwei Chen − *Power Battery & Systems Research Center, State Key Laboratory of Catalysis, Dalian Institute of Chemical Physics, Chinese Academy of Sciences, Dalian 116023, China*; orcid.org/0000-0003-3463-5509; Email: zwchen@dicp.ac.cn

Authors

Jingxuan Ren − *State Key Laboratory of Engineering Materials for Major Infrastructure, School of Materials Science and Engineering, Southeast University, Nanjing 211189, China; Power Battery & Systems Research Center, State Key Laboratory of Catalysis, Dalian Institute of Chemical Physics, Chinese Academy of Sciences, Dalian 116023, China*

Yufeng Chen − *Power Battery & Systems Research Center, State Key Laboratory of Catalysis, Dalian Institute of Chemical Physics, Chinese Academy of Sciences, Dalian 116023, China*

Renming Liu − *Power Battery & Systems Research Center, State Key Laboratory of Catalysis, Dalian Institute of Chemical Physics, Chinese Academy of Sciences, Dalian 116023, China*

Complete contact information is available at: https://pubs.acs.org/10.1021/jacs.6c03001

Notes

The authors declare no competing financial interest.

ACKNOWLEDGMENTS

This work was supported by Strategic Priority Research Program of the Chinese Academy of Sciences (XDB0600400), the Science and Technology Major Project of Liaoning Province (2024JH1/11700013), DICP Innovation Funding (DICP-I202517), Commanding Heights of Science and Technology of Chinese Academy of Sciences (Grant No. LDES15 0000), and the State Key Laboratory of Catalysis (2024SKL-C-002). We acknowledge Vacuum Interconnected Nanotech Workstation (Nano-X), Suzhou Institute of Nano-Tech and Nano-Bionics, Chinese Academy of Sciences, and the Big Data Computing Center of Southeast University, China.

REFERENCES

(1) Wu, L.; Li, Z.; Li, H.; Zhang, J.; Li, Y.; Ren, S.; Fan, Z.; Wang, X.; Li, K.; Liu, Z.; Zhang, J.; Yang, J.; Li, Y. W.; Bo, S.; Zhao, Q. Regulating amine substitution in fluorosulfonyl-based flame-retardant electrolytes for energy-dense lithium metal batteries. *J. Am. Chem. Soc.* **2025**, *147*, 16506−16521.

(2) Fan, Z.; Zhou, X.; Qiu, J.; Yang, Z.; Lei, C.; Hao, Z.; Li, J.; Li, L.; Zeng, R.; Chou, S. Sulfur-rich additive-induced interphases enable highly stable 4.6 V $LiNi_{0.5}Co_{0.2}Mn_{0.3}O_2$||graphite pouch cells. *Angew. Chem., Int. Ed.* **2023**, *62*, No. e202308888.

(3) Zhang, B.; Qu, J.; Chen, J.; Lei, J.; Zheng, Z.; Chen, K.; Fang, Y.; Feng, P.; Luo, D.; Chen, Z.; Guo, X. Revolutionizing battery manufacturing: the role of dry electrode technology in sustainable energy storage solutions. *J. Adv. Mater. Res.* **2026**, *2*, 97−118.

(4) Sammed Khan, A.; Li, Y.; Mustafa, S.; Li, M.; Amine, K.; Luo, D.; Chen, Z. Tailoring solid-state electrolytes via coordination chemistry design for lithium batteries operating in subzero environments. *Renewables* **2025**, *3*, 163−173.

(5) Zheng, Z.; Chen, K.; Fang, Y.; Zhou, H.; Feng, P.; Guo, X.; Zheng, Y. Metal-organic frameworks as multifunctional regulators for zinc anode stability in aqueous energy storage systems. *J. Adv. Mater. Res.* **2025**, *1*, 37−55.

(6) Holoubek, J.; Liu, H.; Wu, Z.; Yin, Y.; Xing, X.; Cai, G.; Yu, S.; Zhou, H.; Pascal, T. A.; Chen, Z.; Liu, P. Tailoring electrolyte solvation for Li metal batteries cycled at ultra-low temperature. *Nat. Energy* **2021**, *6*, 303−313.

(7) Yang, T.; Zheng, Y.; Liu, Y.; Luo, D.; Yu, A.; Chen, Z. Reviving low-temperature performance of lithium batteries by emerging electrolyte systems. *Renewables* **2023**, *1*, 2−20.
(8) Xiao, Y.; He, Q.; Peng, L.; Liu, J.; Guan, X.; Chen, L.; Cai, Y.; Zheng, Q. Synergistic effect of high donor electrolyte and catalytic separator for practical lithium-sulfur batteries. *Renewables* **2024**, *2*, 364−374.
(9) Lai, P.; Zhang, Y.; Wang, J.; Chen, M.; Li, X.; Deng, X.; Chen, Q.; Huang, B.; Gan, C.; Zou, Y.; Qiao, Y.; Zhang, P.; Zhao, J. Adsorption-attraction electrolyte addressing anion-deficient interface for lithium metal batteries. *eScience* **2025**, *5*, No. 100399.
(10) Zhou, X.; Huang, Y.; Wen, B.; Yang, Z.; Hao, Z.; Li, L.; Chou, S. L.; Li, F. Regulation of anion-Na^+ coordination chemistry in electrolyte solvates for low-temperature sodium-ion batteries. *Proc. Natl. Acad. Sci. U.S.A.* **2024**, *121*, No. e2316914121.
(11) Piao, N.; Wang, J.; Gao, X.; Li, R.; Zhang, H.; Hu, G.; Sun, Z.; Fan, X.; Cheng, H.; Li, F. Designing temperature-insensitive solvated electrolytes for low-temperature lithium metal batteries. *J. Am. Chem. Soc.* **2024**, *146*, 18281−18291.
(12) Ma, T.; Ni, Y.; Wang, Q.; Zhang, W.; Jin, S.; Zheng, S.; Yang, X.; Hou, Y.; Tao, Z.; Chen, J. Optimize lithium deposition at low temperature by weakly solvating power solvent. *Angew. Chem., Int. Ed.* **2022**, *61*, No. e202207927.
(13) Cai, G.; Gao, H.; Li, M.; Gupta, V.; Holoubek, J.; Pascal, T. A.; Liu, P.; Chen, Z. Partially ion-paired solvation structure design for lithium-sulfur batteries under extreme operating conditions. *Angew. Chem., Int. Ed.* **2023**, *63*, No. e202316786.
(14) Zhao, Z.; Wang, A.; Chen, A.; Zhao, Y.; Hu, Z.; Wu, K.; Luo, J. Leveraging ion pairing and transport in localized high-concentration electrolytes for reversible lithium metal anodes at low temperatures. *Angew. Chem., Int. Ed.* **2024**, *63*, No. e202412239.
(15) Li, M.; Liu, Y.; Yang, X.; Zhang, Q.; Cheng, Y.; Deng, L.; Zhou, Q.; Cheng, T.; Gu, M. D. Acetonitrile-based local high-concentration electrolytes for advanced lithium metal batteries. *Adv. Mater.* **2024**, *36*, 2404271.
(16) Ma, B.; Zhang, H.; Li, R.; Zhang, S.; Chen, L.; Zhou, T.; Wang, J.; Zhang, R.; Ding, S.; Xiao, X.; Deng, T.; Chen, L.; Fan, X. Molecular-docking electrolytes enable high-voltage lithium battery chemistries. *Nat. Chem.* **2024**, *16*, 1427−1435.
(17) Huang, J.; An, X.; Cheng, Z.; Jiang, J.; Bai, Y.; Liu, H.; Peng, J.; Wu, M.; Dou, S.; Sun, X.; Wu, C. Molecular wedge reconstructing the solvation structure for low-temperature Ah-level anode-free sodium metal batteries. *J. Am. Chem. Soc.* **2025**, *147*, 46594−46607.
(18) Huang, Y.; Fang, H.; Geng, J.; Zhang, T.; Hu, W.; Li, F. Anionic solvation transition at low temperatures for reversible anodes in lithium-oxygen batteries. *J. Am. Chem. Soc.* **2024**, *146*, 26516−26524.
(19) Wang, M.; Yin, L.; Zheng, M.; Liu, X.; Yang, C.; Hu, W.; Xie, J.; Sun, R.; Han, J.; You, Y.; Lu, J. Temperature-responsive solvation enabled by dipole-dipole interactions towards wide-temperature sodium-ion batteries. *Nat. Commun.* **2024**, *15*, 8866.
(20) Sang, X.; Hu, K.; Chen, J.; Wang, Z.; Xu, H.; Huang, Y.; Hu, X. Temperature-inert weakly solvating electrolytes for low-temperature lithium-ion batteries with micro-sized silicon anodes. *Angew. Chem., Int. Ed.* **2025**, *64*, No. e202500367.
(21) Liang, P.; Li, J.; Dong, Y.; Wang, Z.; Ding, G.; Liu, K.; Xue, L.; Cheng, F. Modulating interfacial solvation via ion dipole interactions for low-temperature and high-voltage lithium batteries. *Angew. Chem., Int. Ed.* **2024**, *64*, No. e202415853.
(22) Zhou, P.; Hou, W.; Xia, Y.; Ou, Y.; Zhou, H.; Zhang, W.; Lu, Y.; Song, X.; Liu, F.; Cao, Q.; Liu, H.; Yan, S.; Liu, K. Tuning and balancing the donor number of lithium salts and solvents for high-performance Li metal anode. *ACS Nano* **2023**, *17*, 17169−17179.
(23) Xu, M.; Zhang, B.; Sang, Y.; Luo, D.; Gao, R.; Ma, Q.; Dou, H.; Chen, Z. Bicontinuous-phase electrolyte for a highly reversible Zn metal anode working at ultralow temperature. *Energy Environ. Sci.* **2024**, *17*, 8966−8977.
(24) Gu, R.; Zhang, D.; Xu, S.; Guo, X.; Xiao, Y.; Sheng, Z.; Xu, Q.; Xu, J.; Zhu, S.; Liao, K.; Gong, S.; Shi, P.; Min, Y. Thermoresponsive ether-based electrolyte for wide temperature operating lithium metal batteries. *Nat. Commun.* **2025**, *16*, 5474.
(25) Jiao, Z.; Cai, X.; Wang, X.; Li, Y.; Bie, Z.; Song, W. Trace amount of nitrilotriacetate induced electrolyte evolution and textured surface for stable Zn anode. *Adv. Energy Mater.* **2023**, *13*, 2302676.
(26) Mönich, C.; Andersson, R.; Hernández, G.; Mindemark, J.; Schönhoff, M. Seeing the unseen: Mg^{2+}, Na^+, and K^+ transference numbers in post-li battery electrolytes by electrophoretic nuclear magnetic resonance. *J. Am. Chem. Soc.* **2024**, *146*, 11105−11114.
(27) Zhang, G.; Zhang, T.; Zhang, Z.; He, R.; Wang, Q.; Chi, S. S.; Cui, Y.; Gu, M. D.; Liu, Z.; Chang, J.; Wang, C.; Xu, K.; Deng, Y. High-energy and fast-charging lithium metal batteries enabled by tuning Li^+-solvation via electron-withdrawing and lithiophobicity functionality. *Nat. Commun.* **2025**, *16*, 4722.
(28) Lu, Y.; Zhao, C.; Huang, J.; Zhang, Q. The timescale identification decoupling complicated kinetic processes in lithium batteries. *Joule* **2022**, *6*, 1172−1198.
(29) Yin, X.; Li, B.; Liu, H.; Wen, B.; Liu, J.; Bai, M.; Zhang, Y.; Zhao, Y.; Cui, X.; Su, Y.; Gao, G.; Ding, S.; Yu, W. Solvent-derived organic-rich SEI enables capacity enhancement for low-temperature lithium metal batteries. *Joule* **2025**, *9*, No. 101823.
(30) Li, G.; Koverga, V.; Nguyen, A.; Kou, R.; Ncube, M.; Jiang, H.; Wang, K.; Liao, M.; Guo, H.; Chen, J.; Dandu, N.; Ngo, A. T.; Wang, D. Enhancing lithium-metal battery longevity through minimized coordinating diluent. *Nat. Energy* **2024**, *9*, 817−827.
(31) Choi, I. R.; Chen, Y.; Shah, A.; Florian, J.; Serrao, C.; Holoubek, J.; Lyu, H.; Zhang, E.; Lee, J. H.; Lin, Y.; Kim, S. C.; Park, H.; Zhang, P.; Lee, J.; Qin, J.; Cui, Y.; Bao, Z. Asymmetric ether solvents for high-rate lithium metal batteries. *Nat. Energy* **2025**, *10*, 365−379.
(32) Li, Y.; Mao, E.; Min, Z.; Cai, Z.; Chen, Z.; Fu, L.; Duan, X.; Wang, L.; Zhang, C.; Lu, Z.; Liu, W.; Seh, Z. W.; Sun, Y. Hybrid polymer-alloy-fluoride interphase enabling fast ion transport kinetics for low-temperature lithium metal batteries. *ACS Nano* **2023**, *17*, 19459−19469.
(33) Zhang, H.; Zeng, Z.; Wu, Q.; Wang, X.; Qin, M.; Lei, S.; Cheng, S.; Xie, J. Loosely coordinating diluted highly concentrated electrolyte toward −60 °C Li metal batteries. *J. Energy Chem.* **2024**, *90*, 380−387.
(34) Tan, C.; Shen, Z.; Zhang, S.; Wu, Z.; He, S.; Pan, H.; Cheng, H.; Lu, Y. Methylation design on weakly solvating ethers for wide-temperature Li-SPAN battery. *Adv. Funct. Mater.* **2025**, *35*, 2509658.
(35) Yin, Y.; Holoubek, J.; Kim, K.; Liu, A.; Bhamwala, B.; Wang, S.; Lu, B.; Yu, K.; Gao, H.; Li, M.; Raghavendran, G.; Cai, G.; Li, W.; Liu, P.; Meng, Y. S.; Chen, Z. Coulombic condensation of liquefied gas electrolytes for Li metal batteries at ambient pressure. *Angew. Chem., Int. Ed.* **2024**, *64*, No. e202420411.
(36) Tang, J.; Wei, Z.; Wu, J.; Cui, Z.; Tian, R.; Jiang, H.; Du, F.; Lu, J. Neighboring alkenyl group participated ether-based electrolyte for wide-temperature lithium metal batteries. *Nat. Commun.* **2025**, *16*, 7917.
(37) Wang, Z.; Wang, Y.; He, X.; Geng, M.; Zhang, B. Designing bi-layer electrode-electrolyte interfaces with an asymmetric ether to enable wide-temperature lithium metal batteries. *Nat. Commun.* **2025**, *16*, 10976.
(38) Chen, J.; Lu, H.; Kong, X.; Liu, J.; Liu, J.; Yang, J.; Nuli, Y.; Wang, J. Interphase engineering via solvent molecule chemistry for stable lithium metal batteries. *Angew. Chem., Int. Ed.* **2024**, *63*, No. e202317923.
(39) Ma, T.; Ni, Y.; Li, D.; Zha, Z.; Jin, S.; Zhang, W.; Jia, L.; Sun, Q.; Xie, W.; Tao, Z.; Chen, J. Reversible solid-solid conversion of sulfurized polyacrylonitrile cathodes in lithium-sulfur batteries by weakly solvating ether electrolytes. *Angew. Chem., Int. Ed.* **2023**, *135*, No. e202310761.

https://doi.org/10.1021/jacs.6c03001
J. Am. Chem. Soc. 2026, 148, 19128−19137